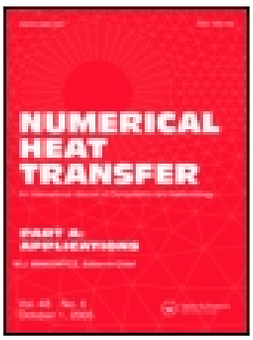

Numerical Heat Transfer, Part A: Applications

ISSN: 1040-7782 (Print) 1521-0634 (Online) Journal homepage: http://www.tandfonline.com/loi/unht20

Natural Convection Heat Transfer in a Porous Rhombic Annulus

F. Moukalled & M. Darwish

To cite this article: F. Moukalled & M. Darwish (2010) Natural Convection Heat Transfer in a Porous Rhombic Annulus, Numerical Heat Transfer, Part A: Applications, 58:2, 101-124, DOI: 10.1080/10407782.2010.497322

To link to this article: http://dx.doi.org/10.1080/10407782.2010.497322

Numerical Heat Transfer, Part A, 58: 101–124, 2010

ISSN: 1040-7782 print/1521-0634 online
DOI: 10.1080/10407782.2010.497322

Taylor & Francis
Taylor & Francis Group

NATURAL CONVECTION HEAT TRANSFER IN A POROUS RHOMBIC ANNULUS

F. Moukalled and M. Darwish
Department of Mechanical Engineering, American University of Beirut, Beirut, Lebanon

Numerical solutions are presented for laminar natural convection heat transfer in a fluid saturated porous enclosure between two isothermal concentric cylinders of rhombic cross-sections. Simulations are conducted for four values of Raleigh number ($Ra = 10^4$, 10^5, 10^6, and 10^7), three values of Darcy number ($Da = 10^{-1}$, 10^{-3}, and 10^{-5}), three values of porosity ($\varepsilon = 0.3$, 0.6, and 0.9), four values of enclosure gap ($E_g = 0.875$, 0.75, 0.5, and 0.25), and two values of Prandtl number ($Pr = 0.7$ and 5). The results are reported in terms of streamlines, isotherms, mid-height velocity and temperature profiles, and local and average Nusselt number values. The flow strength and convection heat transfer increase with an increase in Ra, Da, E_g, and/or ε. At low E_g values, the flow in the enclosure is weak and convection heat transfer is low even though the total heat transfer is higher than at higher E_g values, due to an increase in conduction heat transfer. An increase in Pr is associated with a decrease in the flow strength and an increase in total heat transfer. Furthermore, $\overline{Nu}$ predictions indicate the presence of a critical Ra number below which conduction is the dominant heat transfer mode. Convection starts affecting the total heat transfer at Ra values higher than the critical one. The critical Ra decreases with increasing Da and/or ε, and increases with decreasing E_g.

INTRODUCTION

Temperature-driven flow in porous media arises in a large variety of industrial applications in different fields, such as geothermal energy modeling, thermal insulation material, and solar receivers to cite a few. Most previous studies on free convection in porous media have concentrated on simple rectangular enclosure. Work reported in complex geometries has been rather limited. The focus of the present investigation is on natural convection heat transfer in a porous annulus between two horizontal pipes of a rhombic cross section.

Many researchers have investigated natural convection in rectangular porous enclosures with insulated bottom and top walls and heated/cooled side walls either isothermally or via a uniform heat flux (e.g. [1, 2]). Natural convection heat transfer in a rectangular porous enclosure with a sinusoidal temperature profile on the

Received 2 April 2010; accepted 14 May 2010.
The financial support provided by the University Research Board of the American University of Beirut is gratefully acknowledged.
Address correspondence to F. Moukalled, Department of Mechanical Engineering, American University of Beirut, P.O. Box 11-0236, Riad El Solh, Beirut 1107 2020, Lebanon. E-mail: memouk@aub.edu.lb

NOMENCLATURE

A	wall area	T	dimensional temperature
c_p	specific heat	u, U	dimensional and dimensionless x-velocity component
d_p	pores diameter	v, V	dimensional and dimensionless y-velocity component
D	length of pipe's main diagonal	$\mathbf{v}$, $\mathbf{V}$	dimensional and dimensionless velocity vector
Da	Darcy number	x, y	dimensional coordinates
E_g	enclosure gap ratio	X, Y	dimensionless coordinates
F	constant in Forchheimer's extension	α	thermal diffusivity
$\mathbf{g}$	gravitational acceleration	β	thermal expansion coefficient
h	local convection heat transfer coefficient	μ	dynamic viscosity
$\bar{h}$	average convection heat transfer coefficient	ρ	density
k	fluid thermal conductivity	θ	dimensionless temperature
K	permeability of the porous media	ε	porosity
$\mathbf{n}$	unit vector normal to surface	Ω	rhombus angle
Nu	local Nusselt number		
$\overline{\mathrm{Nu}}$	average Nusselt number		
P	dimensional pressure	**Subscripts**	
p	dimensionless pressure	c	cold wall
Pr	Prandtl number	h	hot wall
Ra	Rayleigh number	i	condition at inner pipe
Q_{conv}	total convection heat transfer	o	condition at outer pipe

bottom wall was numerically studied by Varol et al. [3]. Their results indicated that heat transfer decreases with an increase to the enclosure aspect ratio, and increases with an increase to the amplitude of the sinusoidal temperature profile. Numerical results in a rectangular enclosure partially filled with fluid-saturated porous medium and subjected to a spatially uniform internal heat generation were reported by Kim et al. [4]. Hadim [5] studied natural convection heat transfer in a rectangular porous enclosure saturated with a power-law fluid for the configuration in which the enclosure is heated from the side. Reported results indicated an increase in Nusselt number with a decrease in the power law index and/or an increase in Darcy number. The effect of including viscous dissipation in the energy equation on natural convection heat transfer in a square enclosure filled with fluid-saturated porous medium was analyzed by Costa [6]. Rathish Kumar and Singh [7] reported on the combined effect of Rayleigh number and thermal stratification on the global heat flux in porous cavities of varying aspect ratios. Their results indicated a decrease in the global flux with increasing values of the thermal stratification. Hossain and Wilson [8] analyzed unsteady natural convection heat transfer in a rectangular enclosure filled with a fluid-saturated porous medium heated from below and with internal heat generation. Das and Sahoo [9] used a finite-element method to quantify the effect of several parameters on natural convection heat transfer for a fluid saturated heat generating porous medium in a square enclosure. Pourshaghaghy et al. [10] simulated natural convection in a porous square enclosure by a direct numerical method. In their work, the porous medium was modeled using a random distribution of solid blocks; the Navier-Stokes equations were solved directly without any volume averaging and the energy equation was solved separately for the solid phase and fluid flow. Oztop

[11] reported on natural convection heat transfer in a partially cooled and inclined rectangular porous enclosure. The results generated demonstrated that inclination angle is the dominant parameter on heat transfer. Natural convection results in oblique porous enclosures were reported by Baytas and Pop [12].

Investigators have also reported on natural convection heat transfer in non-rectangular porous enclosures. Rathish Kumar and Shalini [13] studied, using the finite-element method, the effect of surface undulations (i.e., number of waves per unit length) on natural convection in a thermally stratified vertical porous enclosure. Wang [14] determined the critical Rayleigh number of a fluid-saturated porous cylindrical enclosure heated from below by a constant flux. Mahmud and Fraser [15], using the finite-volume method, investigated entropy generation and heat transfer for natural convection heat transfer in a two-dimensional circular enclosure. Rao et al. [16] studied, using a vorticity formulation, natural convection in a vertical cylindrical porous annulus.

Using the finite-element method, numerical results were reported for natural convection heat transfer in trapezoidal [17–19] and triangular [20, 21] porous enclosures. Basak et al. [17] investigated the effect of uniform and nonuniform heating of the bottom wall on natural convection in a trapezoidal porous enclosure. While hydrodynamic and thermal symmetry was maintained with uniform heating, nonuniform heating produced lower overall heat transfer rates but with greater heat transfer rates at the center of the bottom wall. Results reported in references [18, 19], demonstrated the effects on natural convection heat transfer of the inclination angle of the trapezoidal porous cavity for various wall heating. Basak et al. [20, 21] repeated the analysis conducted in reference [17] for an isosceles triangular porous enclosure and proposed correlations for the average Nusselt number in the enclosure as functions of Rayleigh number for various Darcy and Prandtl numbers.

In a previous article, Moukalled et al. [22] reported on the natural convection heat transfer in an annulus between two pipes of rhombic cross section. To the best of the authors' knowledge, results for natural convection heat transfer in the same geometry for the case when the enclosure is filled with a porous matrix have not been reported in the literature, which is the intent of this article.

PHYSICAL MODEL AND GOVERNING EQUATIONS

A schematic of the physical domain under consideration, which represents the annulus between two horizontal concentric pipes of rhombic cross sections, is depicted in Figure 1*a*. Because of symmetry, computations are performed only on the right half of the enclosure. The length of the main diagonal of the inner pipe is D_i, while that of the outer pipe is D_o. The walls of the inner and outer pipes are maintained at the uniform hot and cold temperatures T_h and T_c, respectively. The enclosure is assumed to be filled with a porous material of porosity ε. The difference in temperature between the inner and outer walls creates density variations within the fluid filling the porous enclosure and gives rise to the buoyancy forces that move the flow, which is assumed to be steady, incompressible, and two-dimensional. Moreover, the convective fluid and the porous matrix are assumed to be everywhere in local thermodynamic equilibrium. Non-Darcian terms are included in the conservation equations to better model the physical situation. This includes: (1) the inertia

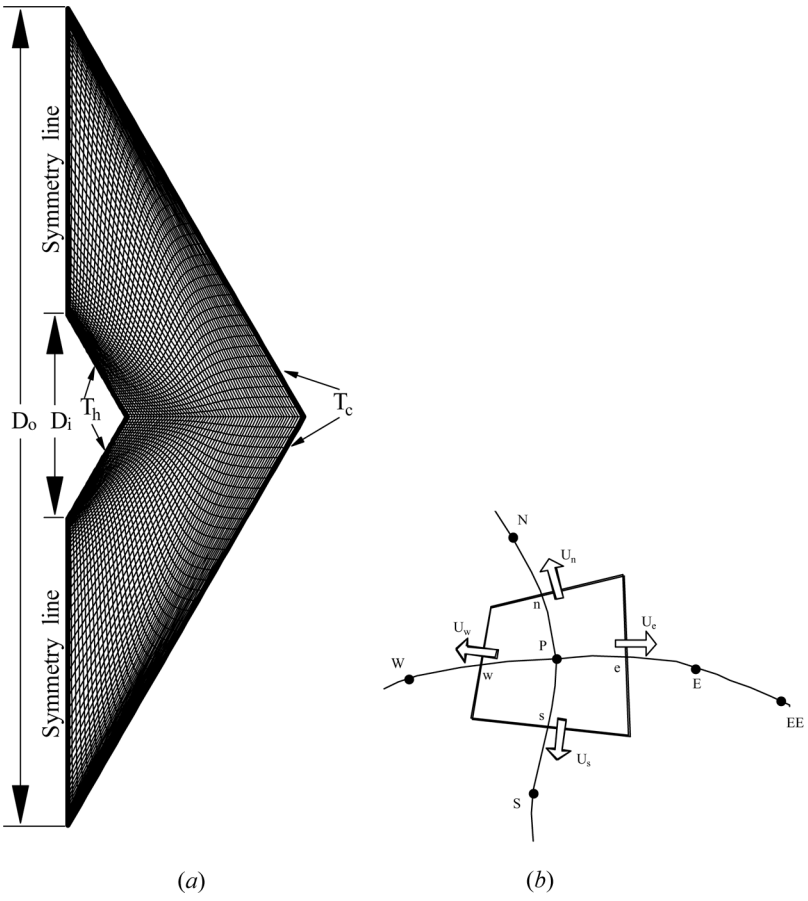

Figure 1. (*a*) Computational domain showing a grid network, and (*b*) a typical control volume.

effect, which is accounted for through the addition of a velocity-squared term in the momentum equation (known as the Forchheimer's extension [23, 24]); and (2) the boundary effect, which may become significant when heat transfer is considered in a region very close to a solid boundary. The Brinkman's extension [25], which incorporates a viscous shear stress term into the momentum equation, together with the no slip boundary condition, is used. With these assumptions, and employing the Boussinesq approximation with the thermophysical properties of the working fluid assumed to be constant, except for density variations in the body force term, the volume-averaged equations [26] governing conservation of mass, momentum, and energy in nondimensional form are, respectively, written as

$$\nabla \cdot \mathbf{V} = 0 \tag{1}$$

$$\frac{1}{\varepsilon^2}(\mathbf{V} \cdot \nabla)\mathbf{V} = \frac{1}{\varepsilon}\sqrt{\frac{\mathrm{Pr}}{\mathrm{Ra}}}\nabla^2\mathbf{V} - \nabla P - \frac{1}{\mathrm{Da}}\sqrt{\frac{\mathrm{Pr}}{\mathrm{Ra}}}\mathbf{V} - \frac{F}{\sqrt{\mathrm{Da}}}|\mathbf{V}|\mathbf{V} + \theta\mathbf{j} \tag{2}$$

$$\mathbf{V} \cdot \nabla\theta = \frac{1}{\sqrt{\mathrm{RaPr}}} \nabla^2\theta \tag{3}$$

with the dimensionless variables defined as

$$\begin{aligned}
&X = \frac{x}{D_o}, \quad Y = \frac{y}{D_o} \\
&U = \frac{u}{\sqrt{g\beta(T_h - T_c)D_o}}, \quad V = \frac{v}{\sqrt{g\beta(T_h - T_c)D_o}}, \quad \mathrm{Da} = \frac{K}{D_o^2} \\
&P = \frac{p + \rho g y}{\rho g \beta (T_h - T_c) D_o}, \quad \theta(x, y) = \frac{T - T_c}{T_h - T_c} \\
&\mathrm{Pr} = \frac{\mu c_p}{k}, \quad \mathrm{Ra} = \frac{\rho g \beta \Delta T D_o^3}{\mu\alpha} \\
&F = \frac{1.75}{\sqrt{150\varepsilon^3}}, \quad K = \frac{\varepsilon^3 d_p^2}{150(1-\varepsilon)^2}
\end{aligned} \tag{4}$$

The meaning of the various dimensionless numbers is given in the nomenclature. The boundary conditions used are

$$U = \frac{\partial V}{\partial X} = \frac{\partial \theta}{\partial X} = 0 \quad \text{along symmetry lines} \tag{5}$$

$$U = V = 0, \ \theta = 1 \quad \text{at inner walls} \tag{6}$$

$$U = V = \theta = 0 \quad \text{at outer walls} \tag{7}$$

SOLUTION PROCEDURE

The system of coupled conservation equations (Eqs. (1)–(3)) subject to the boundary conditions (Eqs. (5)–(7)) is numerically solved using a pressure-based finite-volume method. Solutions are obtained by subdividing the physical domain, depicted in Figure 1*a*, into a finite number of control volumes, each associated with a grid point placed at its geometric center (Figure 1*b*). The partial differential equations (Eqs. (1)–(3)) are integrated over each control volume and profile approximations for the diffusion [27] and convection (the SMART scheme [28], applied within the context of the NVSF methodology [29], is used here) terms are made in each coordinate direction to replace the derivatives by algebraic expressions. The integral value of the source term over a control volume (Figure 1*b*) is evaluated by assuming the source at the control volume center to be equal to the mean value over the whole control volume. The resulting system of algebraic equations is then solved by a block-Thomas algorithm [30]. To evaluate the pressure field, a pressure correction p' ($=p - p^*$, where p^* is the solution from the previous iteration) is defined and a pressure correction equation is derived by combining the momentum and continuity equations as in the SIMPLE procedure of Patankar [30–32]. A collocated grid is used in the present study, and checkerboard pressure and velocity fields are

suppressed through the use of the momentum weighted interpolation method (MWIM) while calculating the mass fluxes across the control volume faces [33].

NUMERICAL ACCURACY AND VALIDATION

Computations are performed using a mesh with a size of 160×128 control volumes. The grid points are unevenly distributed over the domain and concentrated near the walls and symmetry lines where higher gradients are expected (Figure 1*a*). The grid independence of the results was verified by obtaining solutions on a finer mesh, with a size of (240×240) control volumes, and comparing them to the predictions of the coarser mesh (160×128 control volumes). The comparison revealed that the maximum differences in the average Nusselt number values were less than 0.014%. Conservation of the various physical quantities was satisfied to within 10^{-6}% for each control volume.

The correctness of the solution procedure described above is established by comparing results obtained from the present model with corresponding results reported in the literature for various cases. Table 1 compares the average Nusselt number values obtained in a square porous enclosure with similar ones reported by Hadim [34] and Lauriat and Prasad [35]. Figure 2*a* judges the predicted variation in local Nusselt number, along the hot wall of the enclosure, against values reported in reference [34]. Figures 2*b*–2*e* compare streamline and isotherm maps generated in a trapezoidal porous enclosure uniformly heated from the bottom ($\mathrm{Pr} = 0.7$, $\mathrm{Ra} = 10^5$, and $\mathrm{Da} = 10^{-3}$), using the present numerical model with corresponding results reported by Basak et al. [17]. In all cases, a very good agreement is obtained.

RESULTS AND DISCUSSION

The geometric parameters affecting the natural convection heat transfer in this study are the enclosure gap ($E_g = 1 - D_i/D_o$) and the rhombus angle. In order to limit the number of cases to be studied, the rhombus angle is fixed at 30° while the enclosure gap is varied and assigned four different values ($E_g = 0.875$, 0.75, 0.5, and 0.25). On the other hand, the thermophysical parameters in the problem are the porosity (ε), the Rayleigh number (Ra), the Prandtl number (Pr), and the Darcy number (Da). Air and water are considered to be the working fluids and, as such, the Prandtl number is assigned the two values of 0.7 and 5. Moreover, four

Table 1. Comparison of current Nusselt number results with similar ones reported by Hakim [34] and Lauriat and Prasad [35] for a Newtonian fluid in a square porous enclosure ($F = 0.55$)

Ra	Da	Pr	Ref. [34].	Ref. [35].	Present work
10^5	10^{-1}	1	4.38	4.36	4.30
10^5	10^{-1}	10^{-2}	1.90	1.94	1.89
10^8	10^{-4}	1	18.6	18.4	18.39
10^8	10^{-4}	10^{-2}	6.06	6.19	6.04
10^{12}	10^{-8}	1	45.4	44.3	44.16
10^{12}	10^{-8}	10^{-2}	20.0	21.5	21.0

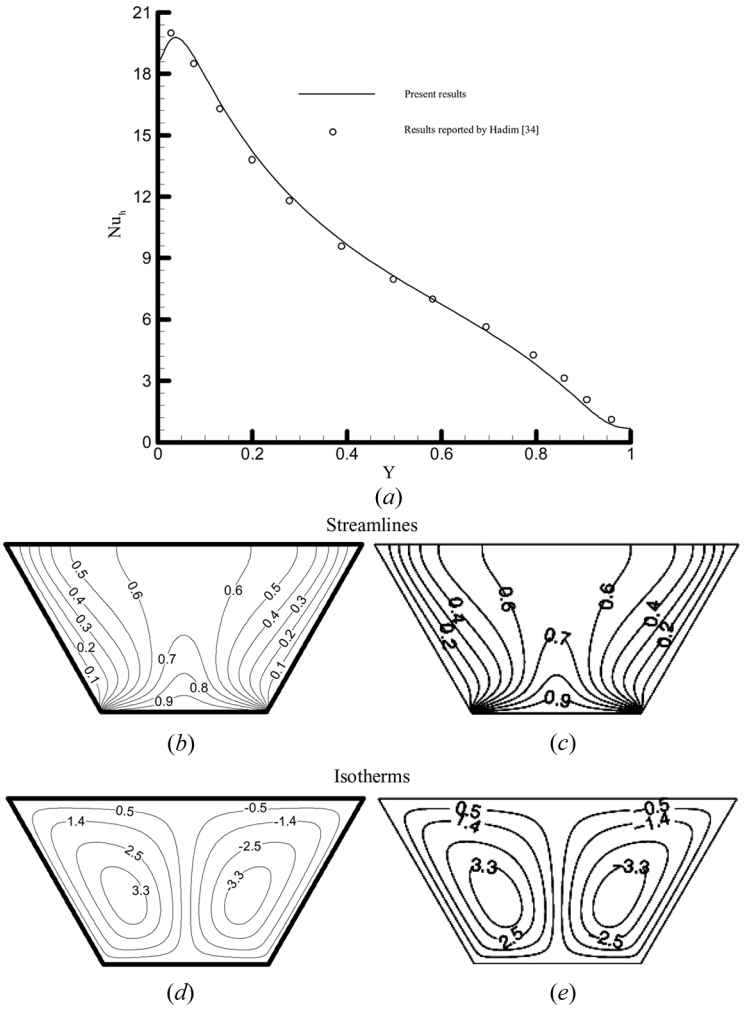

Figure 2. (*a*) Comparison of current local Nusselt number results along the hot wall of a square porous cavity with results reported by Hakim [34]; comparison of streamlines and isotherms generated in a trapezoidal cavity (*b*) and (*d*) with similar ones (*c*) and (*e*) reported in reference [17].

different values of Rayleigh number ($Ra = 10^4$, 10^5, 10^6, and 10^7), three different values of Darcy number ($Da = 10^{-1}$, 10^{-3}, and 10^{-5}), and three different values of porosity ($\varepsilon = 0.3$, 0.6, and 0.9) are considered. Results are presented in the form of streamlines, isotherms, mid-height velocity and temperature profiles, and local and average Nusselt number values.

Streamlines and Isotherms

The influence of the various parameters on the flow and temperature fields is revealed by the streamline and isotherm plots depicted in Figures 3–6. Figure 3

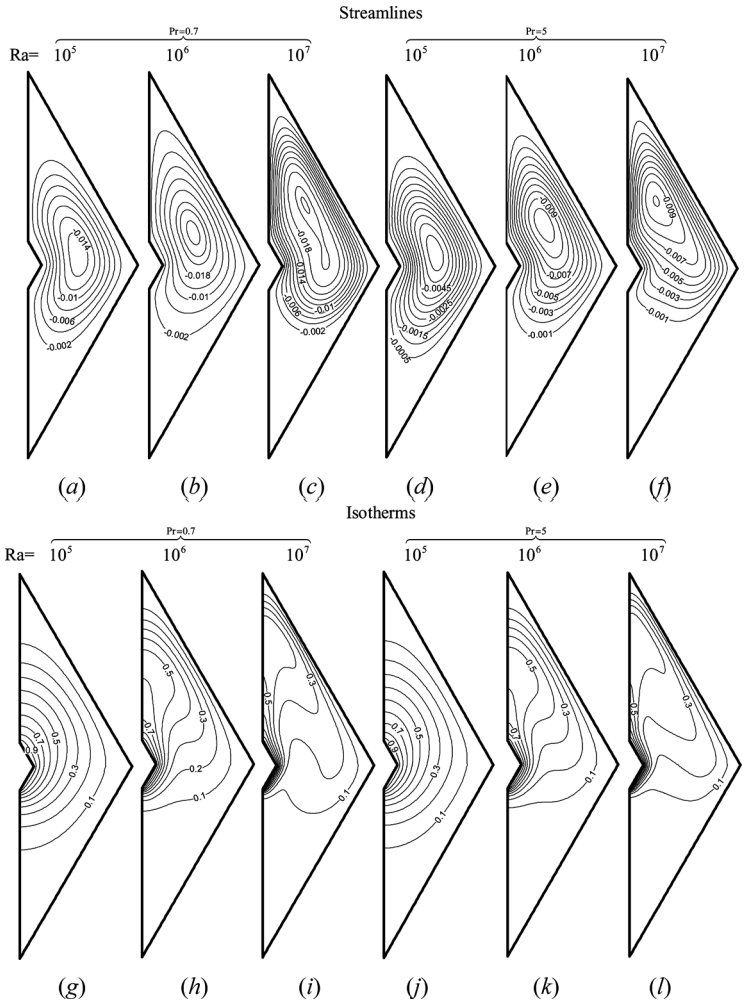

Figure 3. Streamlines and isotherms for different values of Ra number ($E_g = 0.875$, $\varepsilon = 0.6$, and $\mathrm{Da} = 10^{-1}$).

shows the effect of Rayleigh number on natural convection heat transfer in an enclosure with a porosity (ε) value of 0.6, an enclosure gap (E_g) value of 0.875, and a Darcy number (Da) value of 0.1. Streamlines are displayed in Figures 3*a*–3*f*, while isotherms are presented in Figures 3*g*–3*l*. Figures 3*a*–3*c* and 3*g*–3*i* are for a Prandtl number with a value of 0.7; whereas, Figures 3*d*–3*f* and 3*j*–3*l* are for a Prandtl number with a value of 5.

Streamlines indicate that the dominant feature of the flow is a recirculating eddy rotating clockwise with the fluid moving upward adjacent to the inner hot wall and along the symmetry axis, and downward adjacent to the outer cold wall following the contour of the rhombic enclosure. At low Ra value [$\mathrm{Ra} = 10^4$], the flow is weak, and streamlines (Figure 3*a*) and isotherms (Figure 3*f*) tend to be symmetrical across the horizontal diagonal of the enclosure. Moreover, the eye of the

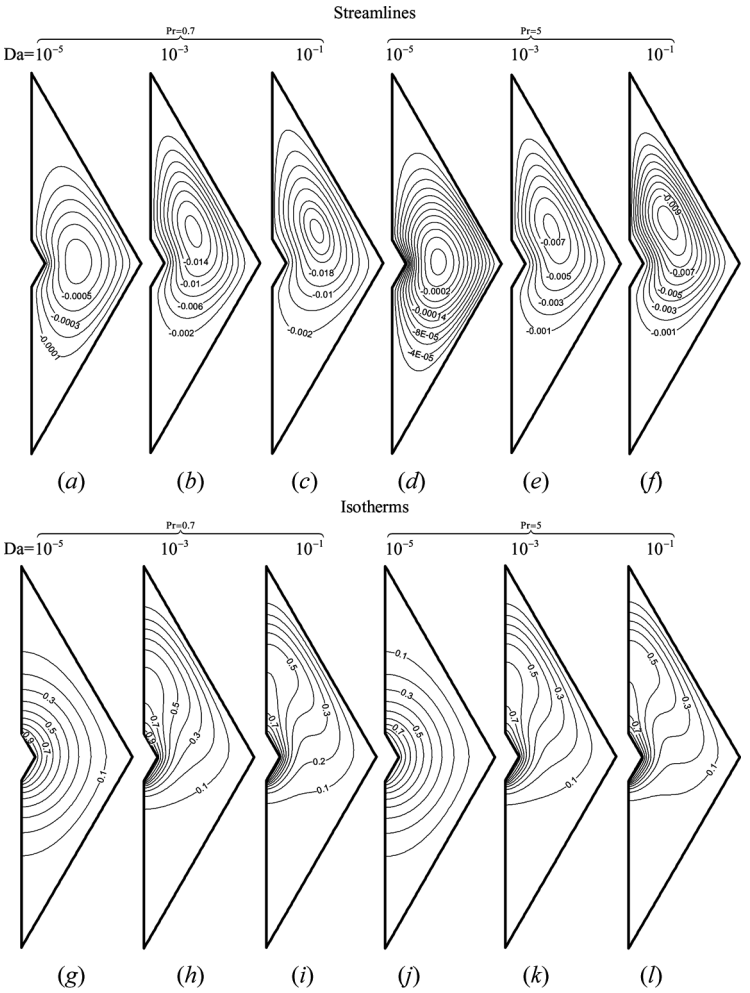

Figure 4. Streamlines and isotherms for different values of Darcy number Da ($E_g = 0.875$, $\varepsilon = 0.6$, and $\mathrm{Ra} = 10^6$).

recirculating eddy is located in the upper half of the domain close to the horizontal centerline of the cavity. As Ra increases (Figures 3*b* and 3*c*), the strength of the flow increases, the isotherm and flow patterns become asymmetrical about the horizontal diagonal, and the eye of eddy moves upward and outward toward the outer cold wall. This behavior is due to the significantly larger area of cold surface relative to the area of hot surface. Below the horizontal diagonal, the cooled surface promotes stratification in the lower half, and above the diagonal, the hot surface promotes stratification in the upper half. Since the lower half is dominated by the much larger cold surface area, there is significant temperature stratification in the lower half, as seen in Figures 3*g* and 3*h*. Because of the thermal stratification in the lower half, the flow cannot easily penetrate the lower region, and as seen in Figures 3*b* and 3*c*, the flow in this region is essentially very weak. In the upper half, due to the relatively

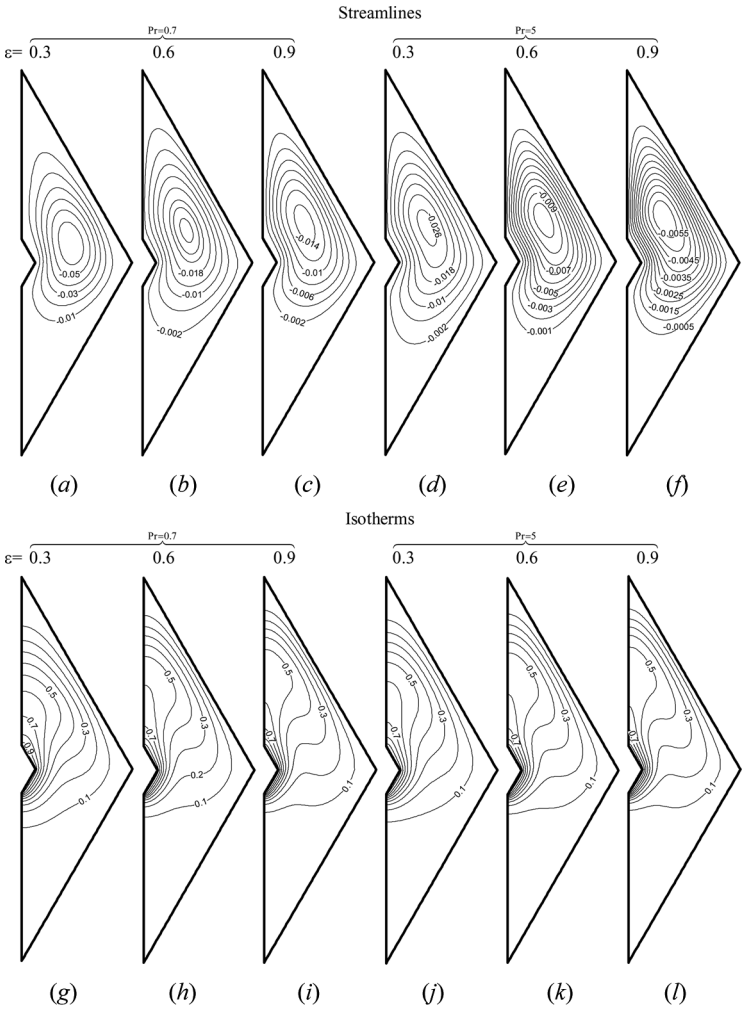

Figure 5. Streamlines and isotherms for different values of porosity ε ($\mathrm{Ra} = 10^6$, $E_g = 0.875$, and $\mathrm{Da} = 0.1$).

lower proportion of hot surface area, stratification is not significant, and a strong recirculating flow is obtained.

Representative streamline plots for $\mathrm{Pr} = 5$ are displayed in Figures 3*d*–3*f*. As compared to results presented in Figures 3*a*–3*c*, a reduction in the flow strength is noticed. This decrease at higher Pr values is due to the higher fluid viscosity which increases the viscous effects and prohibits the fluid near the hot wall from appreciably accelerating. Therefore, the increase in velocity in the layer adjacent to the hot wall is smaller at higher values of Pr, as reflected by the streamlines presented. The corresponding isotherm plots are presented in Figures 3*k* and 3*l*. As expected, the thermal boundary layer decreases in thickness as Pr increases. This is reflected by the denser clustering of isotherms close to the hot outer wall in comparison with corresponding isotherms presented for $\mathrm{Pr} = 0.7$ (Figures 3*h* and 3*i*).

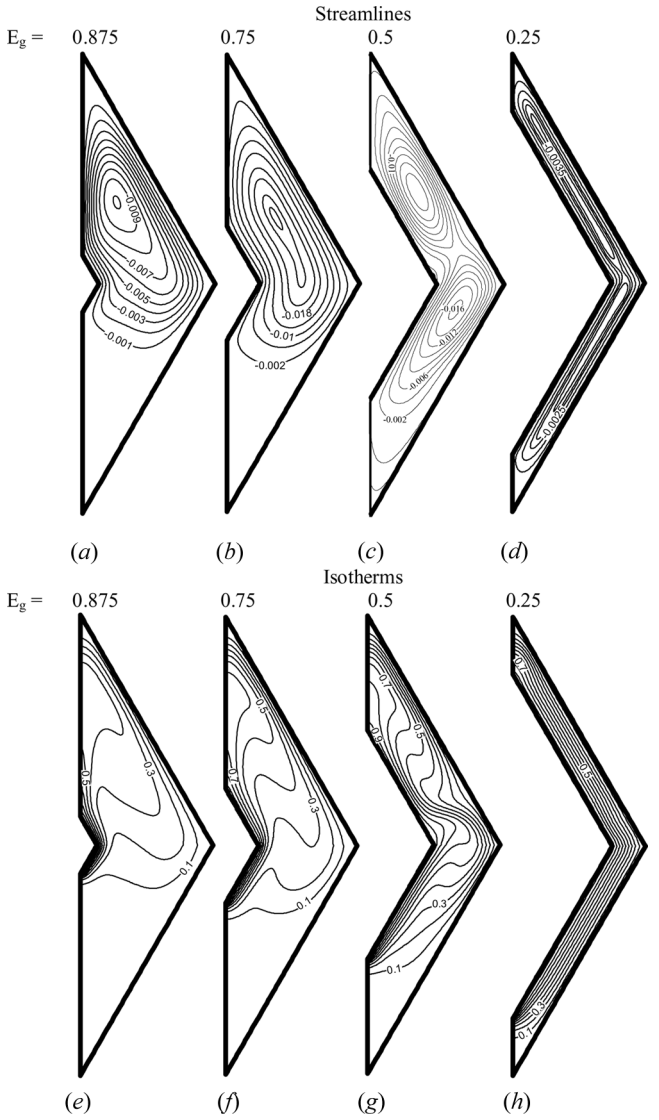

Figure 6. Streamlines and isotherms for different E_g values ($\mathrm{Pr} = 0.7$, $\mathrm{Ra} = 10^7$, $\varepsilon = 0.6$, and $\mathrm{Da} = 0.1$).

The effects of Da on the flow and temperature fields are depicted in Figure 4. Results are presented in an enclosure for which E_g, ε, and Ra have values of 0.875, 0.6, and 10^6, respectively. As shown in Figures 4*a*–4*c*, the strength of the flow increases with increasing values of Da and the eye of the recirculating eddy moves upward and outward toward the outer cold wall. An increase in the Darcy number indicates either an increase in the permeability of the porous matrix or a decrease in the characteristic length. An increase in the permeability of the porous matrix implies lower hydrodynamic resistance and consequently stronger convective flow. At a given Ra value, a decrease in the enclosure characteristic length implies (based on

the definition of Ra) an increase in the temperature difference across the cavity with a consequent increase in the strength of the convective flow. At higher Pr values, streamlines presented in Figures 4*d*–4*f* indicate that the strength of the flow is lower than the corresponding cases displayed in Figures 4*a*–4*c* for the same reasons stated earlier. The corresponding isotherms presented in Figures 4*g*–4*l* indicate an increase in convection contribution to total heat transfer as reflected by the increased asymmetry of isotherms with increasing values of Da and/or Pr.

The hydrodynamic and thermal fields depicted in Figure 5 demonstrate the effects of porosity on natural convection heat transfer in an enclosure for which E_g, Da, and Ra have values of 0.875, 0.1, and 10^6, respectively. Streamlines displayed in Figures 5*a*–5*c* for $\mathrm{Pr} = 0.7$ and in Figures 5*d*–5*f* for $\mathrm{Pr} = 5$ show that the strength of the flow increases with increasing values of ε. This is evident by the movement of the eye of the recirculating eddy upward into the upper half of the domain and outward toward the cold wall as ε increases. A further confirmation of this behavior is demonstrated by the isotherms presented in Figures 5*g*–5*l*, which show increased asymmetry in the temperature distribution as ε increases. This increase in the flow strength as ε increases is due to the overall reduction in damping resistance offered by the porous matrix leading to higher velocity and consequently resulting in steeper temperature gradient.

The effects of E_g on the velocity and temperature fields can be inferred from the results presented in Figure 6 for an enclosure with Ra, ε, and Da assigned the values of 10^7, 0.6, and 0.1, respectively. As E_g decreases, the proportion of the hot to the cold surface area approaches unity, the stratification effects in the lower half of the enclosure become less noticeable (Figures 6*a*–6*c*) until they totally disappear at the lowest E_g value ($E_g = 0.25$, Figure 6*d*), where the flow pattern in the upper and lower halves are similar. The strength of the flow decreases with increasing values of the enclosure gap due to a decrease in the available convective area and due to the greater viscous effects of the added surface area. At high E_g (Figures 6*a* and 6*b*) values, the hydrodynamic field is composed of a single vortex core. As E_g decreases, the flow exhibits two vortex cores within one overall large rotating eddy (see Figures 6*c* and 6*d*). These two inner vortices rotate in the clockwise direction. For $E_g = 0.5$, a very small recirculation bubble is predicted near the middle of the hot wall at the location where the air starts to turn and move along the hot wall in the upper portion.

For $E_g = 0.5$, 0.75, and 0.875, the convective flow strength is significant, and the isotherm plots in Figures 6*e*–6*g* clearly show the boundary layer behavior on the lower part of the heated surface and the upper part of the cooled enclosure surface. The boundary layer along the inner wall rises up from the upper region of the inner body and forms a thermal plume. This can be seen as isotherms move rapidly away from the inner wall near the top. At the lowest E_g (Figure 6*h*), isotherms are uniformly distributed over the domain indicating a conduction dominated heat transfer mode.

Velocity and Temperature Profiles

Figures 7 and 8 show vertical velocity and temperature profiles along the horizontal centerline of the cavity plotted in terms of a dimensionless distance

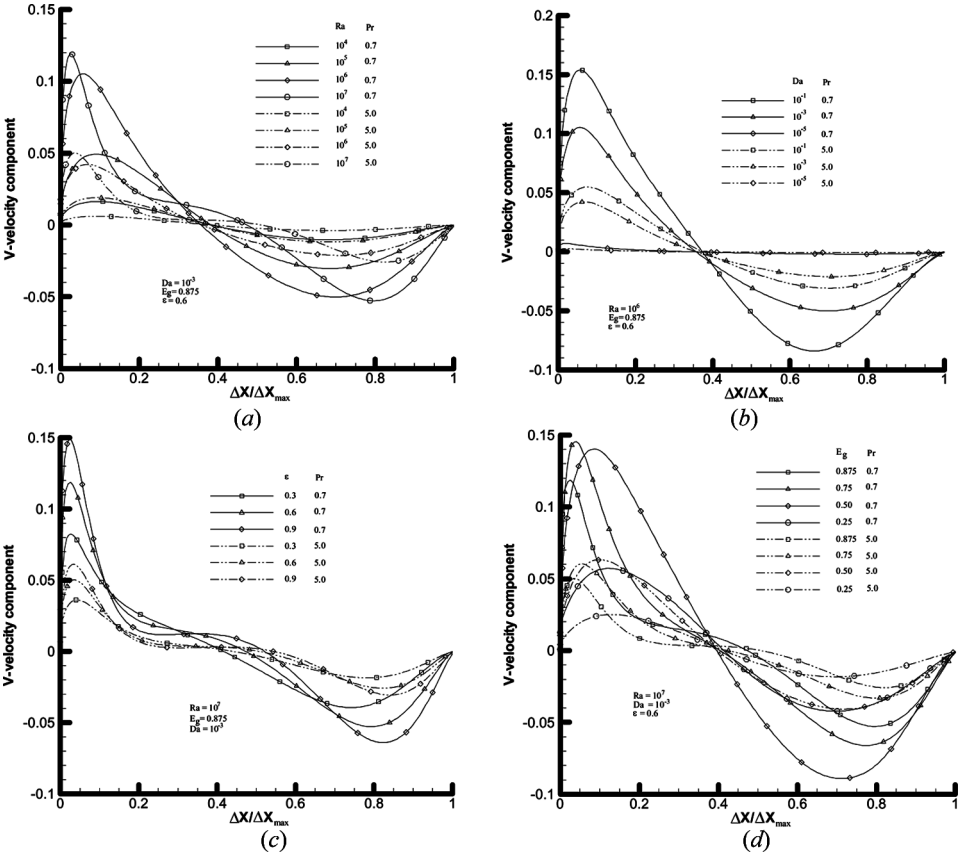

Figure 7. Effect of (*a*) Rayleigh number, (*b*) Darcy number, (*c*) porosity, and (*d*) enclosure gap on mid-height vertical velocity profiles.

$(\Delta X/\Delta X_{\max})$ defined as

$$\frac{\Delta X}{\Delta X_{\max}} = \frac{X - X_{\min}}{X_{\max} - X_{\min}} \tag{8}$$

The effects of Rayleigh number on the V-velocity component are displayed in Figure 7*a*. The peak velocities increase with increasing Ra and occur close to the walls, as expected. The velocity profiles are steeper near the hot wall than near the cold wall. The magnitude of the velocity is very small at low Ra, indicating a heat transfer mode of weak convection and dominant conduction. Profiles at a given Ra obtained for $\mathrm{Pr} = 0.7$ and 5 are similar; nevertheless, the predicted peak values for $\mathrm{Pr} = 5$ are much lower than the corresponding values obtained for $\mathrm{Pr} = 0.7$ because of the higher fluid viscosity at higher Pr values. Results presented in Figure 7*b*, reveal the effects of Da on the V-velocity profiles at the cavity mid-height for a Rayleigh number value of 10^6. As depicted, the peak velocities increase with increasing Da because of the increase in the permeability of the porous matrix

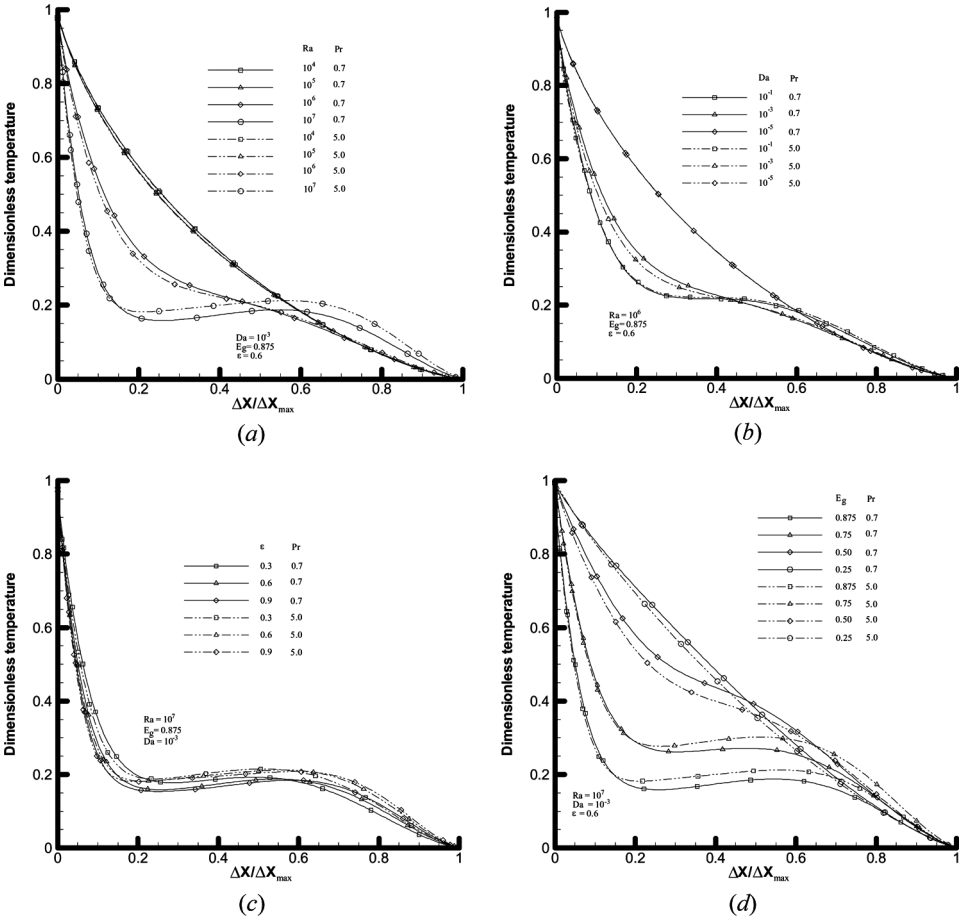

Figure 8. Effect of (*a*) Rayleigh number, (*b*) Darcy number, (*c*) porosity, and (*d*) enclosure gap on mid-height temperature profiles.

and/or the temperature difference across the cavity. Again, the velocity levels decrease with increasing values of Prandtl number for the same reasons stated earlier. The magnitude of the velocity is very small at the lowest Da value ($\mathrm{Da} = 10^{-5}$), indicating a dominant conduction heat transfer mode.

The effects of the porous matrix porosity on the velocity profiles can be inferred from the plots displayed in Figure 7*c* for an enclosure with Da, Ra, and E_g values of 10^{-3}, 10^7, and 0.875, respectively. As shown, the peak velocities increase as the porosity of the cavity is increased leading to a thinner velocity boundary layer and steeper velocity at the walls. The plots also indicate that porosity effects are more pronounced at lower Prandtl number (i.e., variations in the peak V-velocity values are smaller at higher Pr).

Figure 7*d* demonstrates the effects of varying the enclosure gap values on the V-velocity profiles along the horizontal centerline of the cavity. The velocity distributions reflect the streamlines presented in Figure 6. The minimum peak is obtained in

an enclosure with an E_g value of 0.25, corresponding to the lowest enclosure gap considered. As shown in Figure 6*d*, the horizontal diagonal lies in a region of low velocity separating the two vortices formed in the lower and upper parts of the enclosure. As E_g is increased to 0.5, the lower vortex moves upward engulfing the horizontal diagonal and increasing the flow velocity across it. Further increase in E_g to 0.75, forces the two vortices to merge into one with its core located in the upper half of the domain away from the cavity mid-height with a consequent decrease in velocity there. For the largest E_g value ($E_g = 0.875$), the larger convective area promotes higher stratification levels in the lower half of the domain and moves the vortex core up, thereby reducing the velocity along the horizontal diagonal below the values obtained with $E_g = 0.5$ and 0.75, as clearly shown by the profiles plotted in Figure 7*d*.

The corresponding mid-height temperature profiles are shown in Figure 8. The effects of Rayleigh number on temperature are displayed in Figure 8*a*. For high values of Ra, the near-wall region is characterized by a thermal boundary layer, and the temperature profile is characterized by sharp gradients near the hot and cold walls and higher values near the hot wall. The variation in temperature is almost linear at low Ra, indicating conduction as the dominant heat transfer mode. The effects of Pr on temperature are negligible at low Ra (i.e., $\mathrm{Ra} \leq 10^5$) with profiles obtained for $\mathrm{Pr} = 0.7$ and 5 almost on top of each other. The effects of Pr become apparent at high Ra (i.e., $\mathrm{Ra} \geq 10^6$), with temperature profiles close to the cold and hot walls for $\mathrm{Pr} = 5$ being, respectively, above and below the corresponding profiles obtained for $\mathrm{Pr} = 0.7$ indicating higher heat transfer rates.

Results presented in Figure 8*b*, reveal the effects of Da on temperature profiles at the cavity mid-height for $\mathrm{Ra} = 10^6$. Higher temperature gradients near the hot and cold walls are obtained at higher Da values, indicating a stronger convective flow as a result of an increase in the permeability of the porous matrix and/or the temperature difference across the cavity, as explained earlier. For $\mathrm{Da} = 10^{-5}$, the variation in temperature is almost linear and conduction is the dominant heat transfer mode. The Prandtl number effects on temperature become apparent at high values of Da ($\mathrm{Da} \geq 10^{-3}$) with profiles close to the cold and hot walls for $\mathrm{Pr} = 5$ being, respectively, above and below the corresponding profiles obtained for $\mathrm{Pr} = 0.7$ indicating higher heat transfer rates.

The effects of ε on the temperature profiles can be inferred from the plots displayed in Figure 8*c*. As shown, temperature gradients increase with increase to the porosity of the cavity due to the overall reduction in damping resistance offered by the porous matrix. The plots also indicate that the effects of Pr on temperature are significant at all values of ε, leading to higher heat transfer rates at higher Pr values.

Figure 8*d* demonstrates the effects of varying E_g on the temperature profiles along the horizontal centerline of the cavity. As shown, the temperature distortion is stronger at higher enclosure gap values due to the stronger convective flow and temperature gradients near the hot and cold walls. At the lowest enclosure gap, variation in temperature is almost linear and conduction heat transfer is dominant. The effects of Pr on the temperature are significant at all values of E_g with profiles close to the cold and hot walls for $\mathrm{Pr} = 5$ being, respectively, above and below the corresponding profiles obtained for $\mathrm{Pr} = 0.7$, indicating higher heat transfer rates at higher Pr values.

Nusselt Number

The local Nusselt numbers along the inner and outer walls of the porous rhombic annulus are calculated as

$$\left.\begin{array}{ll} \mathrm{Nu}_i = h_i D_i/k & \mathrm{Nu}_o = h_o D_o/k \\ h_i = -k\frac{\nabla T_i \cdot \mathbf{n}}{T_h - T_c} & h_o = -k\frac{\nabla T_o \cdot \mathbf{n}}{T_h - T_c} \end{array}\right\} \Rightarrow \left\{\begin{array}{l} \mathrm{Nu}_i = -\frac{D_i}{D_o}\nabla\theta_i \cdot \mathbf{n} \\ \mathrm{Nu}_o = -\nabla\theta_o \cdot \mathbf{n} \end{array}\right. \tag{9}$$

Furthermore, the average Nusselt number values are defined as

$$\left.\begin{array}{ll} \bar{h}_i = \dfrac{Q_{\mathrm{conv}}}{A_i(T_h - T_c)} & \bar{h}_o = \dfrac{Q_{\mathrm{conv}}}{A_o(T_h - T_c)} \\ Q_{\mathrm{conv}} = \int_i (-k\nabla T_i \cdot \mathbf{n})ds = \int_o (-k\nabla T_o \cdot \mathbf{n})ds & \\ \overline{\mathrm{Nu}}_i = \frac{1}{A_i}\int_i \mathrm{Nu}_i ds & \overline{\mathrm{Nu}}_o = \frac{1}{A_o}\int_o \mathrm{Nu}_o ds \\ A_i = \dfrac{D_i}{\cos\Omega} & A_o = \dfrac{D_o}{\cos\Omega} \end{array}\right\} \Rightarrow \overline{\mathrm{Nu}}_i = \overline{\mathrm{Nu}}_o \tag{10}$$

Therefore, there is no need to give separate attention to $\overline{\mathrm{Nu}}_i$ and $\overline{\mathrm{Nu}}_o$, and attention will subsequently be focused on $\overline{\mathrm{Nu}}$. The local Nusselt number distributions along the hot and cold walls are presented in Figures 9 and 10. Values are plotted as a function of a dimensionless distance ($\Delta Y/\Delta Y_{\max}$) defined as

$$\frac{\Delta Y}{\Delta Y_{\max}} = \frac{Y - Y_{\min}}{Y_{\max} - Y_{\min}} \tag{11}$$

Local Nusselt number profiles along the cold and hot walls presented in Figures 9 and 10 are similar. Profiles along the cold wall exhibit two peaks, one in the lower half of the enclosure ($\Delta Y/\Delta Y_{\max} < 0.5$), and the other in the upper half ($\Delta Y/\Delta Y_{\max} > 0.5$) while passing through a sharp minimum at the middle of the wall ($\Delta Y/\Delta Y_{\max} = 0.5$). The local maximum along the lower part is due to the impingement and deflection of the downward descending fluid by the lower portion of the cold wall. The upper maximum is due to the hot fluid from the inner wall rising upward and impinging on the upper part of the cold wall. The sharp minimum at the corner of the outer cold wall is due to the tendency of the fluid not to follow the corner contour with a consequent decrease in velocity and heat transfer. On the other hand, the Nusselt number along the hot wall peaks near the bottom region ($\Delta Y/\Delta Y_{\max} = 0$), and at the middle of the domain ($\Delta Y/\Delta Y_{\max} = 0.5$), with the latter being sharp. The cooled fluid from the cold wall is transported by the clockwise eddy toward the lower regions of the hot wall, and the largest temperature gradients and Nusselt numbers therefore occur in the leading region of the hot wall, thereby maximizing Nu there. The sharp peak at $\Delta Y/\Delta Y_{\max} = 0.5$ is due to the acceleration of the flow until reaching the tip of the lower part of the hot wall where it has to change direction to turn around the corner. Beyond that point, and because of the increase in temperature of the fluid in the lower part of the hot wall, the rate of heat transfer starts to decrease (i.e., decreasing Nu) while the fluid temperature continues to increase.

The effects of Rayleigh number on the variations of local Nusselt number along the cold and hot walls are displayed in Figures 9*a* and 9*b*, respectively. Along the outer cooled wall (Figure 9*a*), at low Ra ($\mathrm{Ra} \leq 10^5$), the profile is nearly

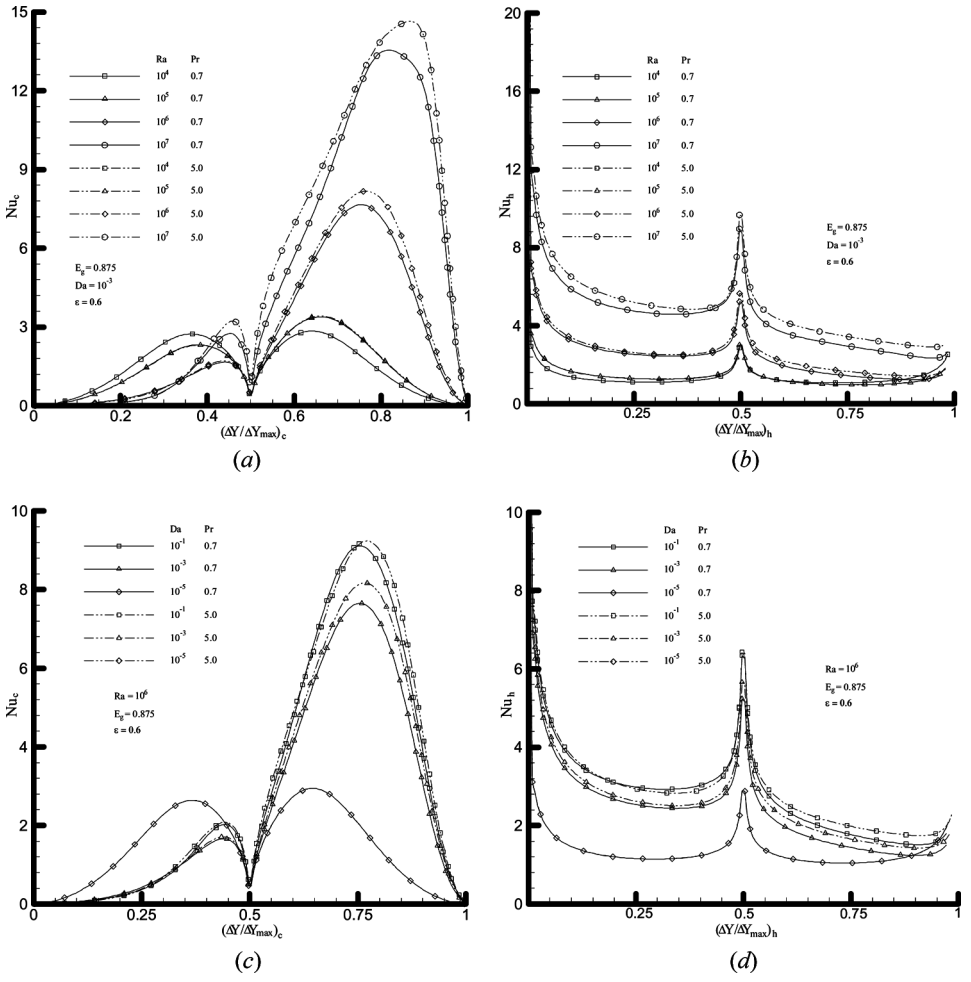

Figure 9. Effect of Rayleigh number on Nusselt number distribution along the (*a*) cold and (*b*) hot walls of the enclosure; effect of Darcy number on Nusselt number distribution along the (*c*) cold and (*d*) hot walls of the enclosure.

symmetrical, reflecting the effects of the symmetrical flow patterns and isotherms shown earlier. The local maximum along the lower region is less than that along the upper region because the upward impinging fluid on the upper cold wall is hotter. As Ra increases ($Ra \geq 10^6$) the lower portion is increasingly thermally stratified, the downward descending flow penetrates the lower region to a lesser degree, and the maximum Nu in the lower region correspondingly decreases. On the other hand, with increasing Ra, the strength of the convective flow increases in the upper portion of the enclosure, and consequently, the Nu peak increases along the upper cold wall. Thus, as Ra increases, most of the heat transfer along the outer cold wall occurs along its upper portion. Nusselt number at the middle of the cold wall is nearly constant and independent of Ra. Along the inner hot wall, the peaks near the bottom

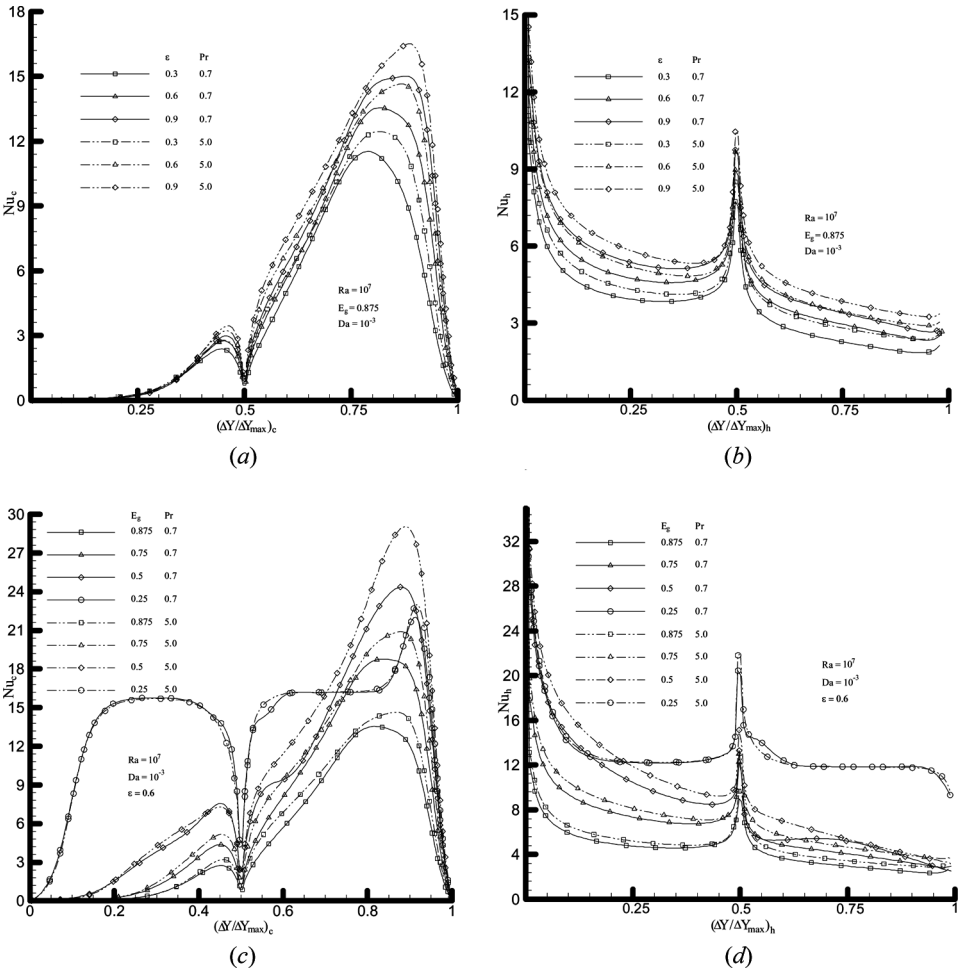

Figure 10. Effect of Porosity on Nusselt number distribution along the (*a*) cold and (*b*) hot walls of the enclosure; effect of enclosure gap ratio on Nusselt number distribution along the (*c*) cold and (*d*) hot walls of the enclosure.

region and at the middle of the domain increase with increasing Ra values because of the stronger convective flow as demonstrated by the streamlines and isotherms presented earlier. Furthermore, results presented in Figures 9*a* and 9*b* demonstrate that the rate of heat transfer increases with increasing Pr, and the rate of this increase is higher at higher Ra.

The effects of Darcy number on the local Nusselt number along the cold and hot walls are presented in Figures 9*c* and 9*d*, respectively. At low Da, the Nu profile along the cold wall (Figure 9*c*) is nearly symmetrical. As Da increases, the strength of the flow in the upper half of the domain increases as a result of the higher permeability, and the thermal stratification in the lower part of the domain increases. This reduces the maximum Nu along the lower part of the cold wall and increases

Table 2. Average Nusselt number values $(\overline{\mathrm{Nu}})$ for $\mathrm{Pr}=0.7$

	$E_g=0.875$			$E_g=0.75$			$E_g=0.5$			$E_g=0.25$		
						$\varepsilon=0.3$						
Ra\Da	10^{-5}	10^{-3}	10^{-1}	10^{-5}	10^{-3}	10^{-1}	10^{-5}	10^{-3}	10^{-1}	10^{-5}	10^{-3}	10^{-1}
10^4	1.45	1.45	1.45	2.28	2.28	2.28	4.99	4.99	4.99	13.06	13.06	13.06
10^5	1.45	1.47	1.49	2.28	2.29	2.30	4.99	4.99	4.99	13.06	13.06	13.06
10^6	1.46	2.07	2.36	2.28	2.79	3.02	4.99	5.09	5.13	13.06	13.06	13.06
10^7	1.75	3.80	4.25	2.54	5.30	5.71	5.08	7.33	8.32	13.07	13.22	13.25
						$\varepsilon=0.6$						
Ra\Da	10^{-5}	10^{-3}	10^{-1}	10^{-5}	10^{-3}	10^{-1}	10^{-5}	10^{-3}	10^{-1}	10^{-5}	10^{-3}	10^{-1}
10^4	1.45	1.45	1.45	2.28	2.28	2.28	4.99	4.99	4.99	13.06	13.06	13.06
10^5	1.45	1.50	1.59	2.28	2.31	2.35	4.99	4.99	5.00	13.06	13.06	13.06
10^6	1.46	2.51	2.98	2.28	3.36	3.96	4.99	5.29	5.49	13.06	13.07	13.07
10^7	1.80	4.61	5.14	2.59	6.62	7.36	5.11	8.79	10.25	13.08	13.60	13.72
						$\varepsilon=0.9$						
Ra\Da	10^{-5}	10^{-3}	10^{-1}	10^{-5}	10^{-3}	10^{-1}	10^{-5}	10^{-3}	10^{-1}	10^{-5}	10^{-3}	10^{-1}
10^4	1.45	1.45	1.46	2.28	2.28	2.28	4.99	4.99	4.99	13.06	13.06	13.06
10^5	1.45	1.53	1.73	2.28	2.33	2.43	4.99	5.00	5.00	13.06	13.06	13.06
10^6	1.46	2.79	3.33	2.28	3.76	4.57	4.99	5.51	5.92	13.06	13.08	13.08
10^7	1.82	5.19	5.63	2.61	7.47	8.31	5.12	10.06	11.48	13.08	14.01	14.27

Table 3. Average Nusselt number values $(\overline{\mathrm{Nu}})$ for Pr = 5

	$E_g = 0.875$			$E_g = 0.75$			$E_g = 0.5$			$E_g = 0.25$		
						$\varepsilon = 0.3$						
Ra\Da	10^{-5}	10^{-3}	10^{-1}	10^{-5}	10^{-3}	10^{-1}	10^{-5}	10^{-3}	10^{-1}	10^{-5}	10^{-3}	10^{-1}
10^4	1.45	1.45	1.45	2.28	2.28	2.28	4.99	4.99	4.99	13.06	13.06	13.06
10^5	1.45	1.47	1.49	2.28	2.29	2.30	4.99	4.99	4.99	13.06	13.06	13.06
10^6	1.46	2.27	2.52	2.28	3.02	3.29	4.99	5.10	5.14	13.06	13.06	13.06
10^7	1.78	4.31	4.49	2.57	6.18	6.53	5.09	8.06	8.56	13.07	13.25	13.26
						$\varepsilon = 0.6$						
Ra\Da	10^{-5}	10^{-3}	10^{-1}	10^{-5}	10^{-3}	10^{-1}	10^{-5}	10^{-3}	10^{-1}	10^{-5}	10^{-3}	10^{-1}
10^4	1.45	1.45	1.45	2.28	2.28	2.28	4.99	4.99	4.99	13.06	13.06	13.06
10^5	1.45	1.50	1.60	2.28	2.31	2.35	4.99	5.00	5.00	13.06	13.06	13.06
10^6	1.46	2.70	3.08	2.28	3.62	4.17	4.99	5.34	5.51	13.06	13.07	13.07
10^7	1.81	5.14	5.32	2.60	7.40	7.80	5.11	10.02	10.82	13.08	13.67	13.74
						$\varepsilon = 0.9$						
Ra\Da	10^{-5}	10^{-3}	10^{-1}	10^{-5}	10^{-3}	10^{-1}	10^{-5}	10^{-3}	10^{-1}	10^{-5}	10^{-3}	10^{-1}
10^4	1.45	1.45	1.46	2.28	2.28	2.28	4.99	4.99	4.99	13.06	13.06	13.06
10^5	1.45	1.53	1.75	2.28	2.33	2.44	4.99	5.00	5.00	13.06	13.06	13.06
10^6	1.46	2.95	3.42	2.28	4.00	4.74	4.99	5.59	5.96	13.06	13.08	13.08
10^7	1.82	5.70	5.92	2.62	8.20	8.66	5.12	11.26	12.25	13.08	14.13	14.28

it along the upper part. The minimum Nu value at the middle of the cold wall is seen to be independent of Da. Along the inner hot wall (Figure 9*d*), an increase in Da increases the level of Nu as a result of a stronger convective flow. Again, the rate of heat transfer increases with increasing Pr.

The effects of porosity on Nu profiles along the cold and hot walls can be inferred from the plots displayed in Figures 10*a* and 10*b*, respectively. As shown, the level of Nusselt number increases with increasing value of ε due to an increase in the available convective area, leading to a lower hydrodynamic resistance. Once more, results indicate an increase in heat transfer with increasing Pr values.

Figures 10*c* and 10*d*, reveal the effects of the enclosure gap on Nusselt number distributions. Results presented in an enclosure with Ra, Da, and ε assigned the values of 10^7, 10^{-3}, and 0.6, respectively, indicate that the Nu levels increase with decreasing E_g values. This increase is due to an increase in the conduction contribution to total heat transfer as a result of the decrease in the width of the enclosure for the same temperature difference. At low E_g ($E_g = 0.25$), the Nu profiles along the hot and cold walls are nearly symmetrical, and as E_g increases convective effects become more important and the profiles become skewed. Plots in Figures 10*c* and 10*d* also demonstrate that an increase in Pr increases heat transfer with its effects being more pronounced at values of E_g for which convection is important.

The average Nu values for all cases studied are given in Table 2 for $\mathrm{Pr} = 0.7$ and in Table 3 for $\mathrm{Pr} = 5$. At the lowest Ra considered, the overall heat transfer $(\overline{\mathrm{Nu}})$ appears to be strongly dominated by conduction. Beyond a certain critical Ra, convection effects become important on the overall heat transfer. As shown in Tables 2 and 3, the critical Ra decreases with increasing Da and/or ε (for the reasons stated earlier), and increases with decreasing E_g. Below the critical Ra, convection effects are weak and although the velocity, temperature, and heat transfer profiles show mild distortion due to the convective flow (Figures 3–6), these effects are not strong enough to substantially change the overall heat transfer. For Ra less than the critical value, the overall heat transfer is much larger at lower enclosure gap values because of the increased heat conduction contribution as a result of smaller gap width for the same temperature difference. At $\mathrm{Pr} = 5$ (Table 3), the predicted $\overline{\mathrm{Nu}}$ values are equal to those obtained for $\mathrm{Pr} = 0.7$ for Ra below the critical value due to a dominant conduction heat transfer mode. When Ra is above the critical value, higher $\overline{\mathrm{Nu}}$ are obtained at higher Pr indicating higher heat transfer rates. This increase in heat transfer is due to a decrease in the thermal boundary layer, which results in higher temperature gradients. The highest $\overline{\mathrm{Nu}}$ value of 14.28 is found for the lowest E_g, and the highest Da, Ra, Pr, and ε. Also, the lowest $\overline{\mathrm{Nu}}$ of 1.45 is attained at the highest E_g, and the lowest Da, Ra, Pr, and ε. Furthermore, when conduction is the dominant heat transfer mode, $\overline{\mathrm{Nu}}$ predictions depend only on E_g.

CONCLUSION

This article reported on a numerical investigation conducted to study laminar natural convection heat transfer in a porous rhombic annulus. Solutions were generated for several values of Raleigh number, Darcy number, porosity, enclosure gap, and Prandtl number. Results demonstrated that the flow strength and the convection

contribution to total heat transfer increase with an increase in Ra, Da, E_g, and/or ε. Conduction heat transfer was found to increase with a decrease in the enclosure gap value. At high E_g values, the flow was found to be composed of a single vortex core; while at low E_g, the flow exhibited two vortex cores within one overall large rotating eddy. Convection promoted thermal stratification below the horizontal diagonal, leading to an increasingly stagnant flow in the lower half of the enclosure. Increasing the Prandtl number resulted in a decrease in the flow strength and an increase in total heat transfer. For a given E_g, Da, ε, and Pr results indicated the existence of a critical Ra below which conduction is the dominant mode of heat transport. The critical Ra decreases with increasing Da and/or ε, and increases with decreasing E_g.

REFERENCES

1. A. Bejan, On the Boundary Layer Regime in a Vertical Enclosure Filled with a Porous Medium, *Letters in Heat and Mass Transfer*, vol. 6, pp. 93–102, 1979.
2. R. J. Gross, M. R. Bear, and C. E. Hickox, The Application of Flux-Corrected Transport (FCT) to High Rayleigh Number Natural Convection in a Porous Medium, *Proc. of the 8th Int. Heat Transfer Conf.*, San Francisco, CA, USA, 1986.
3. Y. Varol, H. F. Oztop, and I. Pop, Numerical Analysis of Natural Convection for a Porous Rectangular Enclosure with Sinusoidally Varying Temperature Profile on the Bottom Wall, *Int. Comm. in Heat and Mass Transfer*, vol. 35, pp. 56–64, 2008.
4. G. B. Kim, J. M. Hyun, and H. S. Kwak, Buoyant Convection in a Square Cavity Partially Filled with a Heat-Generating Porous Medium, *Numer. Heat Transfer A*, vol. 40, pp. 601–618, 2001.
5. H. Hadim, Non-Darcy Natural Convection of a Non-Newtonian Fluid in a Porous Cavity, *Int. Comm. in Heat and Mass Transfer*, vol. 33, pp. 1179–1189, 2006.
6. V. A. F. Costa, On Natural Convection in Enclosures Filled with Fluid-Saturated Porous Media Including Viscous Dissipation, *Int. J. Heat and Mass Transfer*, vol. 49, pp. 2215–2226, 2006.
7. B. V. Rathish Kumar and P. Sigh, Effect of Thermal Stratification on Free Convection in a Fluid-Saturated Porous Enclosure, *Numer. Heat Transfer A*, vol. 34, pp. 343–356, 1998.
8. M. A. Hossain and M. Wilson, Natural Convection Flow in a Fluid-Saturated Porous Medium Enclosed by Non-Isothermal Walls with Heat Generation, *Int. J. Thermal Sci.*, vol. 41, pp. 447–454, 2002.
9. S. Das and R. K. Sahoo, Effect of Darcy, Fluid Rayleigh and Heat Generation Parameters on Natural Convection in a Porous Square Enclosure: A Brinkman-Extended Darcy Model, *Int. Comm. in Heat and Mass Transfer*, vol. 26, no. 4, pp. 569–578, 1999.
10. A. Pourshaghaghy, A. Hakkaki-Fard, and A. Mahdavi-Nejad, Direct Simulation of Natural Convection in Square Porous Enclosure, *Energy Conversion and Management*, vol. 48, pp. 1579–1589, 2007.
11. H. F. Oztop, Natural Convection in Partially Cooled and Inclined Porous Rectangular Enclosures, *Int. J. Thermal Sci.*, vol. 46, pp. 149–156, 2007.
12. A. C. Baytas and I. Pop, Free Convection in Oblique Enclosures Filled with a Porous Medium, *Int. J. Heat and Mass Transfer*, vol. 42, pp. 1047–1057, 1999.
13. B. V. Rathish Kumar and Shalini, Natural Convection in a Thermally Stratified Wavy Vertical Porous Enclosure, *Numer. Heat Transfer A*, vol. 43, pp. 753–776, 2003.
14. C. Y. Wang, Onset of Natural Convection in a Fluid-Saturated Porous Medium Inside a Cylindrical Enclosure Bottom Heated by Constant Flux, *Int. Comm. in Heat and Mass Transfer*, vol. 25, no. 4, pp. 593–598, 1998.

15. S. Mahmud and R. A. Fraser, Free Convection and Irreversibility Analysis Inside a Circular Porous Enclosures, *Entropy*, vol. 5, pp. 358–365, 2003.
16. V. Dharma Rao, S. V. Naido, and P. K. Sarma, Non-Darcy Effects in Natural Convection Heat Transfer in a Vertical Porous Annulus, *Journal of Heat Transfer*, vol. 118, pp. 502–505, 1996.
17. T. Basak, S. Roy, A. Singh, and I. Pop, Finite Element Simulation of Natural Convection Flow in a Trapezoidal Enclosure Filled with Porous Medium Due to Uniform and Non-Uniform Heating, *Int. J. Heat and Mass Transfer*, vol. 52, pp. 70–78, 2009.
18. T. Basak, S. Roy, S. K. Singh, and I. Pop, Finite Element Simulation of Natural Convection within Porous Trapezoidal Enclosures for Various Inclination Angles: Effect of Various Wall Heating, *Int. J. Heat and Mass Transfer*, vol. 52, pp. 4135–4150, 2009.
19. T. Basak, S. Roy, A. Singh, and A. R. Balakrishnan, Natural Convection Flows in Porous Trapezoidal Enclosures with Various Inclination Angles, *Int. J. Heat and Mass Transfer*, vol. 52, pp. 4612–4623, 2009.
20. T. Basak, S. Roy, S. K. Babu, and I. Pop, Finite Element Simulations of Natural Convection Flow in an Isosceles Triangular Enclosure Filled with a Porous Medium: Effects of Various Thermal Boundary Conditions, *Int. J. Heat and Mass Transfer*, vol. 51, pp. 2733–2741, 2008.
21. T. Basak, S. Roy, and S. K. Babu, Natural Convection and Flow Simulation in Differentially Heated Isosceles Triangular Enclosure Filled with Porous Medium, *Chem. Eng. Sci.*, vol. 63, pp. 3328–3340, 2008.
22. F. Moukalled, H. Diab, and S. Acharya, Laminar Natural Convection in a Horizontal Rhombic Annulus, *Numer. Heat Transfer A*, vol. 23, pp. 101–119, 1993.
23. K. Vafai and C. L. Tien, Boundary and Inertia Effects on Flow and Heat Transfer in Porous Media, *Int. J. Heat and Mass Transfer*, vol. 24, pp. 195–203, 1981.
24. X. B. Chen, P. Yu, S. H. Winoto, and H. T. Low, Free Convection in a Porous Wavy Cavity Based on the Darcy–Brinkman–Forchheimer Extended Model, *Numer. Heat Transfer A*, vol. 52, pp. 377–397, 2007.
25. H. C. Brinkman, On the Permeability of Media Consisting of Closely Packed Porous Particles, *Appl. Sci. Res.*, vol. 1, pp. 81–86, 1947.
26. A. Amiri and K. Vafai, Analysis of Dispersion Effect, and Non-Thermal Equilibrium, Non-Darcian Variable Porosity Incompressible Flow through Porous Media, *Int. J. Heat and Mass Transfer*, vol. 37, pp. 939–954, 1994.
27. P. J. Zwart, G. D. Raithby, and M. J. Raw, An Integrated Space-Time Finite-Volume Method for Moving-Boundary Problems, *Numer. Heat Transfer B*, vol. 34, pp. 257–270, 1998.
28. P. H. Gaskell and A. K. C. Lau, Curvature Compensated Convective Transport: SMART, a New Boundedness Preserving Transport Algorithm, *Int. J. for Numer. Meth. in Fluids*, vol. 8, pp. 617–641, 1988.
29. M. Darwish and F. Moukalled, Normalized Variable and Space Formulation Methodology for High-Resolution Schemes, *Numer. Heat Transfer B*, vol. 26, pp. 79–96, 1994.
30. S. V. Patankar, *Numerical Heat Transfer and Fluid Flow*, Hemisphere Publishing Corporation, New York, 1980.
31. F. Moukalled and M. Darwish, Pressure Based Algorithms for Single and Multifluid Flow, in W. J. Minkowycz, E. M. Sparrow, and J. Y. Murthy (eds.), *Handbook of Numerical Heat Transfer*, 2nd edition, pp. 325–367, Wiley, New York, 2006.
32. F. Moukalled and M. Darwish, A Unified Formulation of the Segregated Class of Algorithms for Fluid Flow at All Speeds, *Numer. Heat Transfer B*, vol. 37, no. 1, pp. 103–139, 2000.

33. M. Peric, A Finite Volume Method for the Prediction of Three-Dimensional Fluid Flow in Complex Ducts, Ph.D. Thesis, Imperial College, Mechanical Engineering Department, London, UK, 1985.
34. H. Hadim, Non-Darcy Natural Convection of a Non-Newtonian Fluid in a Porous Cavity, *Int. Comm. in Heat and Mass Transfer*, vol. 33, pp. 1179–1189, 2006.
35. G. Lauriat and V. Prasad, Non-Darcian Effects on Natural Convection in a Vertical Porous Enclosure, *Int. J. Heat and Mass Transfer*, vol. 32, pp. 2135–2148, 1989.